



HAL
open science

Study of a Rock-Ramp Fish Pass with Staggered Emergent Square Obstacles

Flavia Cavalcanti Miranda, Ludovic Cassan, Pascale Laurens, Tien Dung Tran

► **To cite this version:**

Flavia Cavalcanti Miranda, Ludovic Cassan, Pascale Laurens, Tien Dung Tran. Study of a Rock-Ramp Fish Pass with Staggered Emergent Square Obstacles. *Water*, 2021, 13 (9), pp.1175. 10.3390/w13091175 . hal-04124013

HAL Id: hal-04124013

<https://ut3-toulouseinp.hal.science/hal-04124013v1>

Submitted on 9 Jun 2023

HAL is a multi-disciplinary open access archive for the deposit and dissemination of scientific research documents, whether they are published or not. The documents may come from teaching and research institutions in France or abroad, or from public or private research centers.


L'archive ouverte pluridisciplinaire **HAL**, est destinée au dépôt et à la diffusion de documents scientifiques de niveau recherche, publiés ou non, émanant des établissements d'enseignement et de recherche français ou étrangers, des laboratoires publics ou privés.



Distributed under a Creative Commons Attribution 4.0 International License

Article

Study of a Rock-Ramp Fish Pass with Staggered Emergent Square Obstacles

Flavia Cavalcanti Miranda ¹, Ludovic Cassan ^{1,*} , Pascale Laurens ¹ and Tien Dung Tran ²

¹ Fluid Mechanics Department Laboratory, Institut de Mécanique des Fluides, Allée du Professeur Camille Soula, 31400 Toulouse, France; flavia.cavalcantimiranda@toulouse-inp.fr (F.C.M.); pascale.laurens@imft.fr (P.L.)

² Faculty of Water Resources Engineering, Hanoi Campus (Headquarters), Thuyloi University, No. 175 Tay Son, Dong Da, Hanoi 116705, Vietnam; tientd@tlu.edu.vn

* Correspondence: lcassan@imft.fr

Abstract: A rock-ramp fish passage with square obstacles was experimentally and numerically studied in this work with the objective of investigating in detail the hydraulic behind such fishways and to evaluate the importance of the shape of the obstacles. The LES and VOF methods were used for the simulations, and for the measurements, shadowgraphy and ADV were applied. Two different validations were successfully performed. In the first one, the experimental and numerical results of a chosen case were compared in detail. In the second validation, the focus was given to the stage-discharge. Following the validation, a numerical study was carried out to point out the differences in the flow characteristics from a configuration with square and circular obstacles. The discharge was nearly the same for both configurations, which implies different water depths. The results showed a lower velocity field, lower turbulent kinetic energy, and lower lateral fluctuations for the configuration with square blocks, which indicated a better passability for this geometry. However, it also presented a higher water depth, which led to a less attractive discharge. The differences in the flow generated in the two configurations indicated that the shape is an important modifiable parameter to be considered in the design process.

Keywords: rock-ramp fish passage; large eddy simulation; staggered emergent square obstacles; stage-discharge analysis; experimental validation



Citation: Miranda, F.C.; Cassan, L.; Laurens, P.; Tran, T.D. Study of a Rock-Ramp Fish Pass with Staggered Emergent Square Obstacles. *Water* **2021**, *13*, 1175. <https://doi.org/10.3390/10.3390/w13091175>

Academic Editor: Laurent David

Received: 16 March 2021

Accepted: 17 April 2021

Published: 24 April 2021

Publisher's Note: MDPI stays neutral with regard to jurisdictional claims in published maps and institutional affiliations.



Copyright: © 2021 by the authors. Licensee MDPI, Basel, Switzerland. This article is an open access article distributed under the terms and conditions of the Creative Commons Attribution (CC BY) license (<https://creativecommons.org/licenses/by/4.0/>).

1. Introduction

Rock-ramp fish passes are an economical and ecological alternative to unobstructed fish migrations and contribute to the good ecological condition of the rivers. They generally consist of a sloped bottom in which obstacles are staggered, arranged with the objective of providing energy dissipation and reducing flow velocity [1,2]. The obstacles also provide resting places for fishes swimming upstream [3]. This type of passage is especially interesting due to the high flow, which enhances the attractiveness for fish and decreases the risk of clogging (large spacing between blocks) and silting (no pool) [2].

Fish passes can only have an effective functionality, i.e., reduce the interruptions of fish migration and re-establish the connectivity along the waterways, if they present the adequate flow characteristics related to the fish preferences. For this reason, detailed investigations, both numerical and experimental, about the hydraulic behavior in such passages are essential for their successful design. Some flow characteristics such as turbulence intensity, turbulent kinetic energy, Reynolds stress, vorticity, and eddy sizes have been identified to play an important role in a functional fish pass [4–6].

In the last decade, studies investigating turbulent characteristics in rock-ramp-type fishways have been intensified. Oerte et al. [7] studied the effect of boulder interaction processes with respect to the drag forces and coefficients. The authors pointed out that the wake interaction significantly affects the flow. Later on, Baki et al. [3,8] conducted an

experimental study in a rock-ramp fish pass with a staggered arrangement of boulders to analyze the turbulence characteristics and the wake interference generated. Besides that, Baki et al. [9] provided detailed measurements of the mean and turbulent flow around a boulder under the effect of wake interaction. Exploring the topic of wake interference as well, recently, Golpira et al. [10] presented a study about the effects of boulder spacing and the boulder submergence ratio on the near-bed shear stress, and Golpira et al. [11] provided an experimental study investigating the higher order velocity moments, turbulence time, length scales, and energy dissipation rates around a boulder.

The flow characteristics present in a fish passage are essentially a tridimensional phenomenon, and despite its inherent higher costs, the use of 3D turbulent models is fundamental to effectively reproduce flows with such complexity. Only relatively few 3D numerical studies investigating the turbulence generated in rock-ramp fish passes can be found in the literature. Among them, the studies of Baki et al. [12] and Chorda et al. [1] can be cited. Baki et al. [12] studied the flow characteristics for variations in channel slopes and boulder sizes, spacing, and patterns by using the Reynolds-averaged Navier–Stokes (RANS) methodology. They applied the $k - \epsilon$ as a turbulence model and the volume of fluid (VOF) method to treat the multiple phases. Furthermore, using the VOF, Chorda et al. [1] presented a study of this type of fish pass comparing the turbulence methodology RANS with the shear stress transport (SST) $k - \omega$ model and large-eddy simulation (LES) with the Smagorinsky model. The authors demonstrated that both methodologies were able to capture the underlying physics well and predict the motion of flow features of the studied configuration. Moreover, they pointed out the advantages of employing LES for obtaining more detailed flow characteristics, especially in the wake zone.

Among the works found in the literature, spherical or semi-spherical boulders were mainly used [3,8–12] others employed cylindrical obstacles [1], while square-shaped obstacles were barely used. In this sense, the purpose of this work was to investigate, in detail, the hydraulics behind such a ramp fishway with staggered arranged emergent square blocks and evaluate the importance of the shape of the obstacles in such a configuration. Tseng et al. [13] investigated numerically the differences in the turbulent field around a square and a circular pier. They reported the flow patterns were similar for both cases, but the strengths of the downflow and horseshoe vortex were different. Furthermore, it is known that the shape of the obstacle plays an important role in the resistance forces acting in the flow. In particular, it is expected that the square blocks may reduce the maximal velocity in fish passes for a given slope and block density. However, the eventual differences in the turbulent field due to the shape of the obstacles with the additional effect of boulder interaction processes for a rock-ramp-type fish passage are still unclear.

This study was performed by applying the VOF model, and in order to obtain a more detailed turbulent flow characteristics, LES was employed to model the turbulence. In the first part of this paper, two different investigations were performed to demonstrate the feasibility of the methods, procedures, and assumptions applied in the present study, where the numerical results were compared with measured data. Then, in the second part, the flow characteristics generated in a fish passage with square-shaped obstacles were compared with the flow generated with an array of circular-shaped obstacles. To complete this study, the impact of the identified flow differences on the fish passability was discussed. The results of the present investigation can be helpful for the optimization and designing of rock-ramp fish passages.

2. Description of the Cases of Study

The present paper studied a rock-ramp-type fish pass and was based on the channel studied by Cassan et al. [2] and Chorda et al. [1]. The experimental device consisted of a 1 m width and a 7 m-long flume with its bottom covered with obstacles, as shown in Figure 1. The channel slope could vary from 1% to 7%, and the total discharge could be set from 0.01 to 0.06 m³/s.



Figure 1. Picture of the flume in operation.

The obstacles were staggered arranged in the channel bottom at a spatial concentration of $C = 16\%$, C defined as $C = D^2/a_x a_y$ and D the width of the blocks. The distance between blocks in the longitudinal (a_x) and transverse (a_y) directions, as shown in Figure 2, was $a_x = a_y = 0.285$ m. The obstacles had a square shape with a side length (D) of 0.115 m and a height of 0.15 m. Moreover, Lines 1, 2, and 3 shown in Figure 2 indicate the positions of the measurement and the water flows in the x -direction.

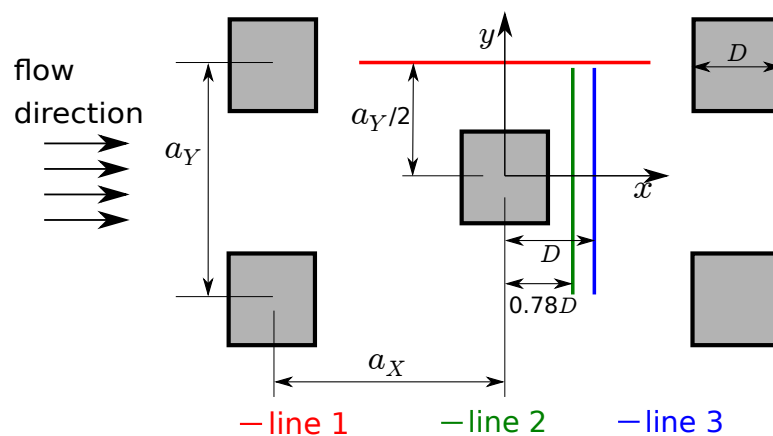


Figure 2. Details of the geometry and position of the collected profiles.

In order to numerically investigate such a problem, this work employed a geometry of a 1 m width and a 0.22 m height with square piers in the same spatial concentration ($C = 16\%$). A representation of the domain can be seen in Figure 3. As in Chorda et al. [1], the flow was considered to be in a state of equilibrium in the zone of interest, i.e., resistance forces and friction losses were balanced by the gravitational force. This assumption together with the periodicity of the pier arrangement of the geometry allowed the application of a cyclic boundary condition and a drastic reduction of the computational domain. Thus, as indicated in Figure 3, the computational domain had a length of 0.570 m. Furthermore, the above-mentioned Lines 1, 2 and 3 were located around the highlighted block shown in Figure 3.

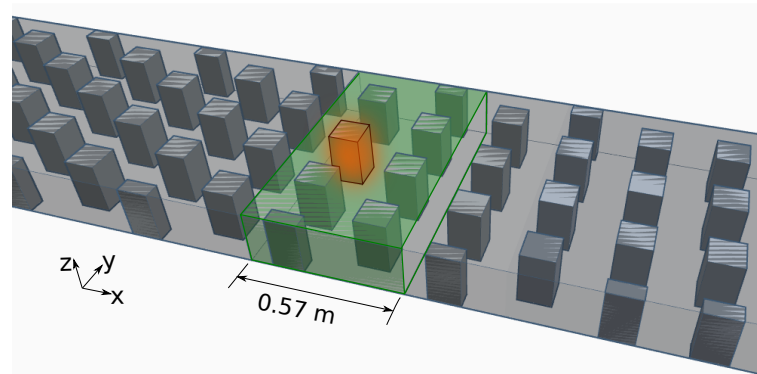


Figure 3. 3D view of the computational domain.

The slope effect was applied by decomposing the gravity into longitudinal $g\sin(\theta)$ and vertical $g\cos(\theta)$ components, with $\theta = \arctan(S)$ and S the considered slope. The calculations were started by setting up a static velocity field and an initial water depth. Because of the imposed gravity, the flow was then accelerated and achieved an equilibrium state, in which the flow properties were collected. This statistic stationary state was determined by the value of the discharge at the cyclic boundary, which gradually increased from zero to equilibrium. The applied initial water depth was set up in the way that the desired flow discharge was reached. Due to mass conservation, the average water height remained as the imposed initial water height.

As in Tran et al. [14] and in Chorda et al. [1], an average velocity between blocks V_g was used as a reference. It is defined as:

$$V_g = \frac{V_0}{1 - \sqrt{\frac{a_x C}{a_y}}} \quad (1)$$

where V_0 is the bulk velocity calculated as $V_0 = Q/(Bh)$, B is the channel width, and h corresponds to the water depth. As done in Cassan et al. [2], the Reynolds and Froude numbers were computed based on V_g , being $Re = V_g D/\nu$ and $F = V_g/\sqrt{gh}$, respectively.

2.1. Validation: Case 1

As a first step, a validation was performed in which one chosen configuration was investigated in detail, and the numerical results were compared with measurements. The configuration with volumetric flow rate $Q = 0.04 \text{ m}^3/\text{s}$ and slope $S = 4\%$ was taken into consideration. This chosen configuration corresponded to the one described in the work of Tran et al. [14], but with square obstacles instead of circular cylinders.

For the numerical investigation, the mean water height measured experimentally ($h = 0.137 \text{ m}$) was set as the initial water depth, and after reaching an equilibrium value, an average discharge of $Q = 0.038 \text{ m}^3/\text{s}$ was obtained. Table 1 shows the main characteristics for this validation case.

Table 1. Setup for validation Case 1.

	Experiment	Simulation
Discharge Q (m^3/s)	0.040	0.038
Water depth h (m)	0.137	0.137
Velocity between blocks V_g (m/s)	0.49	0.46
Reynolds number	56,000	53,000
Froude number	0.42	0.40

2.2. Validation: Case 2

A second validation was carried out by analyzing the stage-discharge relationship for a larger range of Froude numbers. Here, the numerical results were once more compared with the measurements. The stage-discharge relationship was analyzed by focusing on the drag coefficient, which links water depth and discharge. For the experiments, the discharges and the slope were set, then the mean water depth was measured. For the numerical simulations, the water depth and slope were imposed, while the mean discharge was calculated. The applied equation for this analysis is described in Section 3.4

For the measurements, the channel longitudinal slope was varied from 1 to 7%, and the discharge varied from 0.01 to 0.06 m³/s. The Froude number, based on V_g , varied from 0.25 to 0.62. For the numerical simulations, the slope was maintained at 5%, which corresponded to the most common recommendation for this kind of fish pass [15]. The initial water depth was set from 0.06 to 0.2 m. The Froude number, based on V_g , varied for the simulations from 0.38 to 0.64. The main characteristics of the measurements and simulations used for this validation are summarized in Appendix A.

2.3. Comparison between Square and Circular Obstacles

This investigation focuses on the differences in the flow properties between a channel covered with circular and square obstacles. For this aim, a case with circular obstacles computed by Chorda et al. [1] was reproduced, but with square obstacles. Then, both LES results were compared and analyzed. The corresponding volumetric flow rate was $Q = 0.05 \text{ m}^3/\text{s}$, and the slope $S = 5\%$. The initial water depth applied was 0.158 m, delivering an average discharge of $Q = 0.051 \text{ m}^3/\text{s}$. Table 2 summarizes the main characteristics of this case.

Table 2. Setup for the investigation of the differences between square and circular obstacles.

	Circular *	Square
Discharge Q (m ³ /s)	0.052	0.051
Initial water depth h (m)	0.1	0.158
Velocity between blocks V_g (m/s)	0.83	0.53
Reynolds number	95,000	61,000
Froude number	0.83	0.42

* from Chorda et al. [1].

3. Methodologies

3.1. Experimental Methods

Similarly to [2] for circular obstacles, the water depth was measured by shadowgraphy. Then, the mean value was deduced by averaging the pictures in the longitudinal direction.

The experimental measurements of velocity profiles were performed with an acoustic Doppler velocimeter (ADV) with a 3D downlooking probe in which the three velocity components were captured at a frequency of 50 Hz over 180 s. The measurement was carried out on a plane at 3 cm from the bed. It was checked that the velocity was approximately uniform in the vertical direction, except in the block wake. The measurement positions are indicated in Figure 4 by the origin of the velocity vector in red.

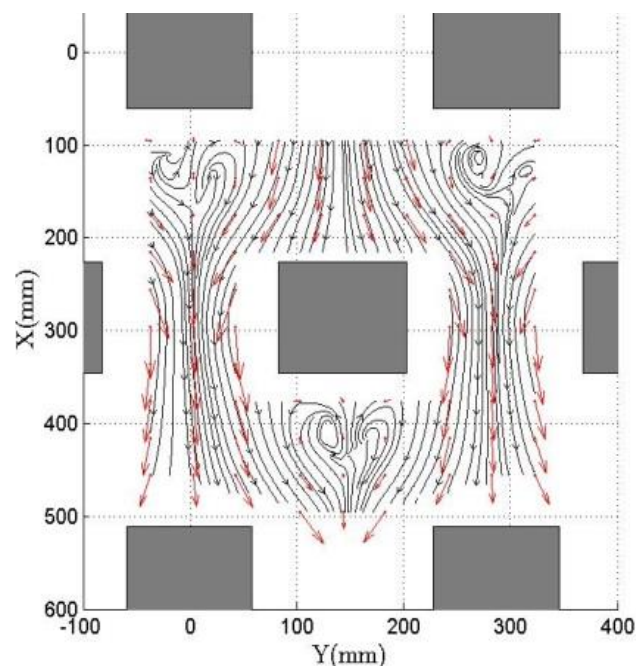


Figure 4. Streamline from the ADV measurement and velocity vectors in red.

3.2. Numerical Methods

The simulations were performed using the two-phase flow solver *interFoam* of the open-source C++ library *OpenFOAM* v1812. It solves the Navier–Stokes equations by applying the pressure-velocity PIMPLE (merged PISO-SIMPLE) correction procedure. For turbulence modeling, this work employed LES with the subgrid-scale model Smagorinsky [16].

InterFoam is a solver applied for two incompressible, isothermal, immiscible fluids and is based on the volume of fluid (VOF) method [17]. In this method, a species transport equation is calculated in each computational cell to determine the relative volume fraction of the two evolved phases, which is called phase fraction α [18]. The local density and viscosity were determined using volume-weighted average found from the α field. It assumed values between zero and one. For the present work, $\alpha = 0$ corresponded to a cell containing 100% air and $\alpha = 1$ to water. To illustrate the phase fraction, Figure 5 shows the instantaneous value of α in a slice at $y = 0.5$ m for the first validation problem. In this case, the water phase covered approximately 65% of the computational domain.

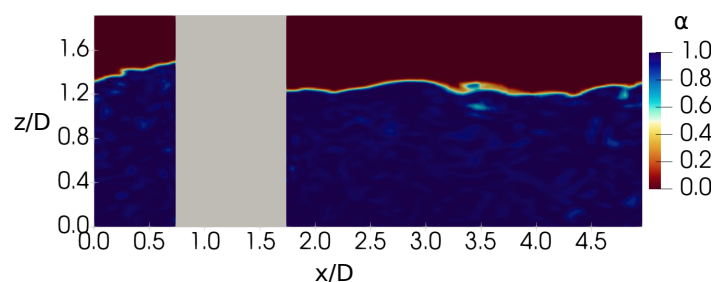


Figure 5. Side view of the phase fraction α along the obstacle center axis.

In the present study, cyclic boundary conditions were applied to the inlet and the outlet, while the wall condition with the wall function was employed for the bottom, obstacles, and side walls. Due to the cyclic boundary conditions, this work employed a modified version of the solver *interFoam*, given in Chorda et al. [1]. Besides that, an explicit first-order Euler integration method was applied for the time derivative terms. The variable time step option available in *OpenFOAM* was used with the maximum global and interface Courant numbers set to 1.0. Moreover, the mean values were obtained by averaging the instantaneous data over 20 s in a sampling frequency of 100 s^{-1} .

3.3. Numerical Grids

The grid used in this study corresponded to a 3D mesh composed of prismatic volumes, created by employing the open-source software SALOME Version 9.3.0. As in Chorda et al. [1], the mesh was obtained by vertical extrusion of a 2D unstructured mesh consisting of triangular volumes. Because of the cyclic boundary condition applied at the inlet and outlet, special attention was given when building the mesh for these two faces. As required in OpenFOAM, they were built as perfect clones. The grid refinement was based on the meshes used in Chorda et al. [1]. Characteristics of the mesh used in this work are given in Table 3.

Table 3. Mesh characteristics.

Characteristics	Values
Size of the domain (mm)	$570 \times 1000 \times 220$
Maximum cell size (mm)	5
Local cell size (mm)	2
Cell height (mm)	2
Total number of volumes	5.9×10^6

3.4. Stage-Discharge Analysis

Following Cassan et al. [2], the momentum balance for a fluid volume around one block in steady and uniform condition, in which the bed friction was neglected, can be written as:

$$C_d \frac{Ch}{D} F^2 = 2S(1 - \sigma C), \quad (2)$$

where C_d is the total drag coefficient of an infinitely long obstacle at a low Froude number, F is the Froude number based on the velocity between blocks V_g , and σ is a shape factor ($\sigma = 1$ for square blocks and $\sigma = \pi/4$ for circular blocks).

In Cassan et al. [19], the total drag coefficient C_d was expressed as a function of two corrective functions $f_F(F)$ and $f_{h_*}(h_*)$, which were used to represent the modification of the free surface and the interaction between the flow and the bed, respectively. In [2,14,19,20], a complete description of these functions for circular obstacles was provided. They depend on the characteristics of the macro-roughness elements and on the conveyance velocity V_0 . However, the validity of these functions for square blocks has not yet been investigated. As a consequence, the stage-discharge analysis was performed only by considering the total drag coefficient C_d .

3.5. Quadrant Analysis

This analysis was based on the sign of the velocity fluctuations of the longitudinal (u') and vertical (w') directions. It was performed to identify and characterize turbulent events [21]. For Quadrant 1, in which $u' > 0$ and $w' > 0$, outward interactions took place. Quadrant 2, in which $u' < 0$ and $w' > 0$, corresponded to ejection events. In Quadrant 3, where $u' < 0$ and $w' < 0$, inward interactions occurred. Finally, Quadrant 4 was where $u' > 0$ and $w' < 0$ and sweep events took place.

As done in Golpira et al. [10,11], the contributions of each quadrant were evaluated by taking into consideration a threshold hole size H ,

$$H = \frac{|u'w'|}{|u'|} \quad (3)$$

In accordance with previous studies [10,11,21], a hole size of $H = 2$ was used in this work to remove insignificant events.

The frequency of each turbulent event $P_{i,H}$ can be computed by [11]:

$$P_{i,H} = \frac{\int_0^T |u'w'| I_{i,H}(u', w') dt}{\int_0^T |u'w'| dt} \quad (4)$$

where T is the total time in which the data were collected, i corresponds to the quadrant number, and I is a conditional function given as [11]:

$$I_{i,H}(u', w') = \begin{cases} 1 & \text{if } (u', w') \text{ is in quadrant } i \text{ and } |u'w'| \geq H|\overline{u'w'}|; \\ 0 & \text{otherwise.} \end{cases} \quad (5)$$

4. Results

4.1. Validation: Case 1

Figure 6 shows the components of the mean velocity along Line 1 for numerical and experimental results. In both results, the axial component u increased from approximately $0.01 V_g$ to $1.3 V_g$, then it slowly decreased to $0.85 V_g$. These values mean that the flow between blocks was contracted in the vertical and span-wise direction. The maximum velocity is a key point for passability and can imply the design choices.

The maximum mean u value along Line 1 was given at $x/D = 0.01$, which was slightly after the center of the reference block. Moreover, as expected, the lateral velocity component v had relatively small values along this line. The maximum value of this component, in absolute, was $0.10 V_g$ for the numerical solution and $0.16 V_g$ for the experimental profile. This line was supposed to present a symmetric axis in which the values would oscillate around zero. However, due to the sidewalls of the scale model, it was not the case for both experimental and numerical results. It is interesting to note that the numerical simulation can also reproduce this particular behavior. Furthermore, the vertical component w also presented relatively small values, i.e., they were in absolute lower than $0.07 V_g$ for the measurements and lower than $0.11 V_g$ for the numerical prediction. Small differences could be seen between the numerical and experimental results, but overall, they agreed well for the three components, giving a good representation of the flow between obstacles.

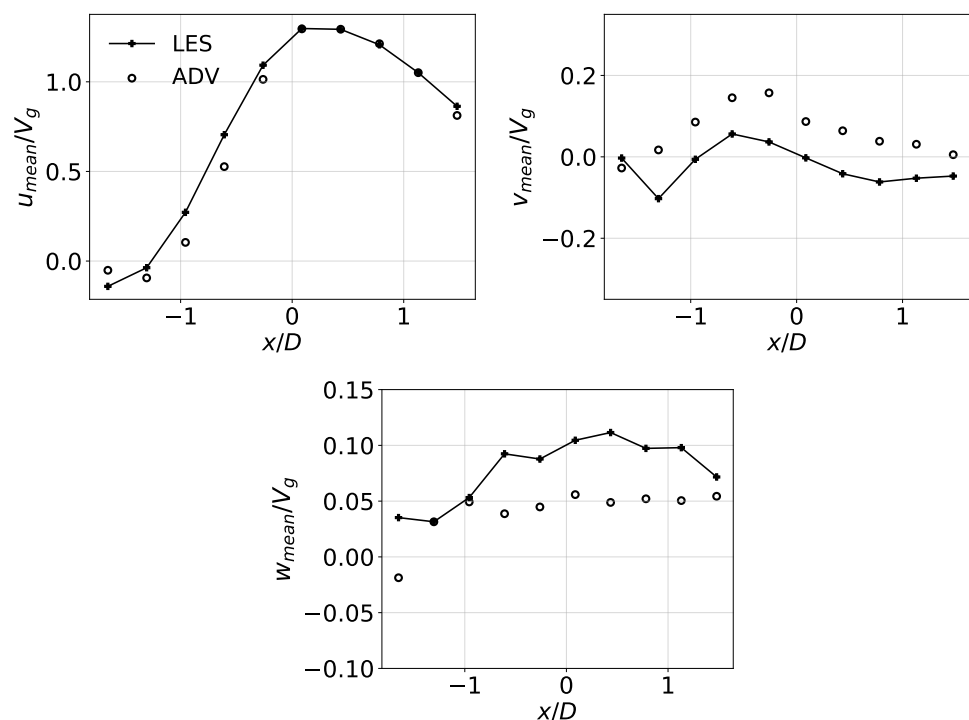


Figure 6. Numerical and experimental mean velocity components along Line 1 at plane $z/h = 0.22$.

The results for the extracted Line 2 located at the wake zone were also in good agreement with the measurements, as can be seen in Figure 7. For both results, the greater values for the axial velocity component ($\approx 1.2 V_g$) were located on the sides of the block. Furthermore, as for the extracted Line 1, the values for the lateral and vertical velocity components were relatively small, being in absolute value less than $0.25 V_g$ and $0.10 V_g$, respectively. The agreement was less good than for Line 1 because in Line 2, there was a strong turbulent point, for $y/D = 0$, where the mean velocity was relatively low. Figures 6 and 7 indicate that the wake zone was slightly shorter in the simulation. For instance, a positive vertical velocity in the numerical simulation for $y/D = 0$ can be observed, which represents the end of the wake zone, whereas the measured velocity was still zero.

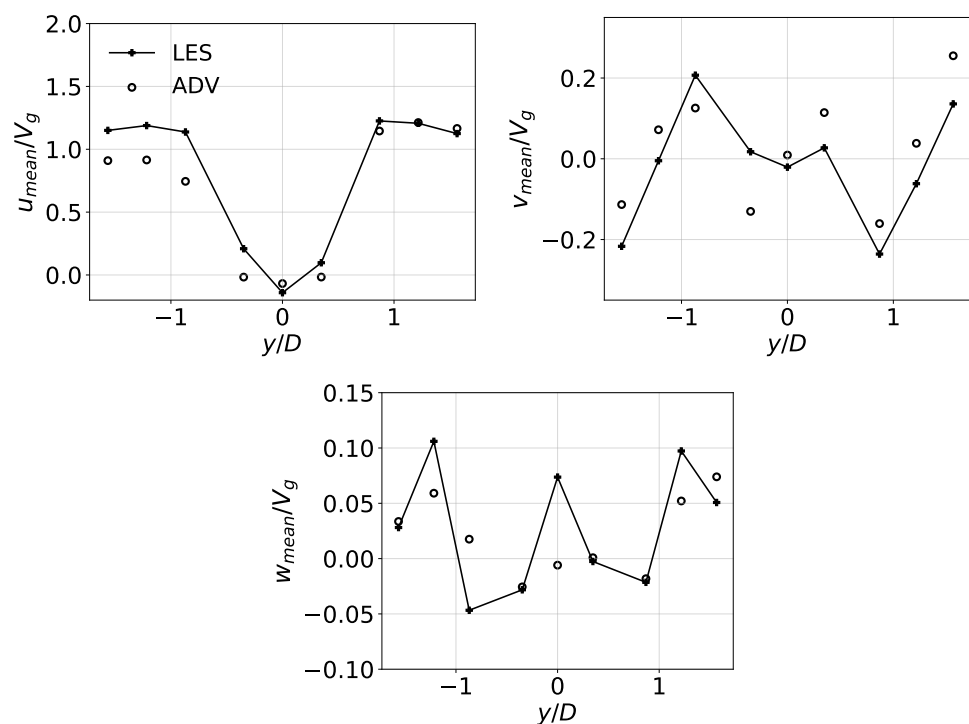


Figure 7. Numerical and experimental mean velocity components along Line 2 at plane $z/h = 0.22$.

Turbulent kinetic energy (k) profiles for Lines 1 and 2, calculated as $k = \frac{1}{2}(\overline{(u')^2} + \overline{(v')^2} + \overline{(w')^2})$, are shown in Figure 8. They reached approximately $0.16 V_g^2$ between the blocks (Line 1) and oscillated around $0.1 V_g^2$ at the wake zone (Line 2). As for the velocities profiles, minor discrepancies could be found, but the numerical results and the measurements had similar values and behavior. As discussed before, the discrepancies can be justified by a shorter wake zone from the numerical results, while exhibiting similar hydrodynamic characteristics.

Spectral analysis of the turbulent kinetic energy at two points located at the wake zone can be seen in Figure 9. These points were located in the center axis of the obstacle of reference. Both spectra displayed regions with a slope of $-5/3$ at a higher Strouhal number ($St > 1$). This indicated a good representation of the smallest scale fluctuations in the simulation, supporting the assumption of an accurate LES. Furthermore, Pope's criterion [22] was also applied to confirm that the size of the employed grid was satisfactory for the LES framework. In most of the domain, at least 85% of the turbulent kinetic energy was solved in the simulation. This value decreased to 80% at the water-air interface and to 75% in the region close to the upstream corners of the obstacles.

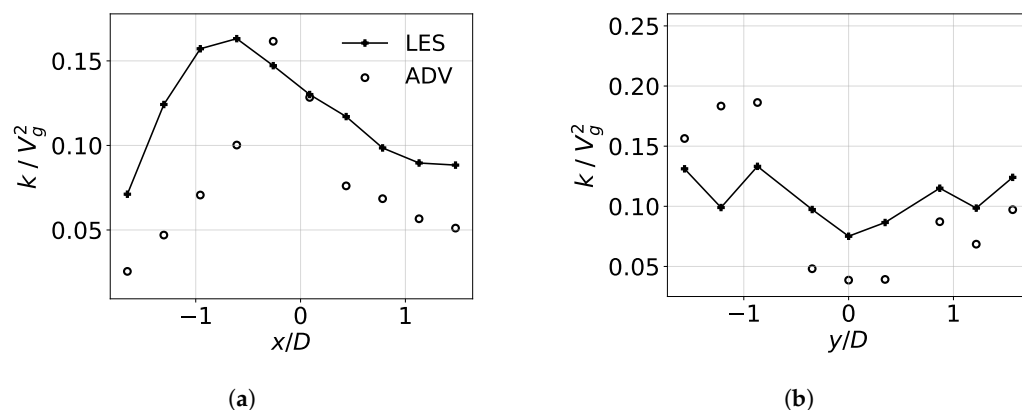


Figure 8. Numerical and experimental turbulent kinetic energy at plane $z/h = 0.22$ along Lines 1 (a) and 2 (b).

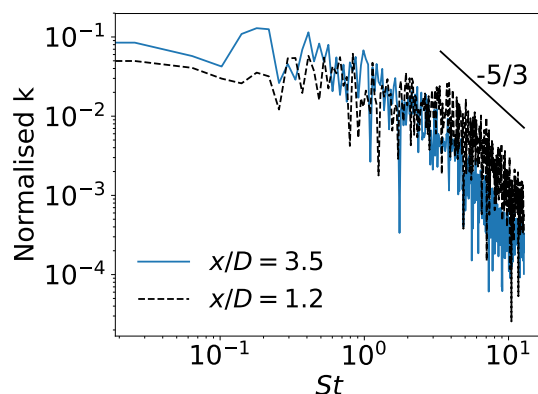


Figure 9. Spectrum of turbulent kinetic energy as a function of the Strouhal at two points located in the center axis of the obstacle of reference.

Different 3D structures can be identified by observing the instantaneous isosurface of the Q-criterion shown in Figure 10. For instance, structures as horseshoe vortices were identified upstream of the obstacles, and lateral vortices could be found in both sides of the blocks. As described in several studies [23–25], these are typical structures found on flows around 3D bed-mounted obstacles. The lateral vortices had relatively low intensity and may show a suitable zone for fish to pass from the wake zone to the upstream block row.

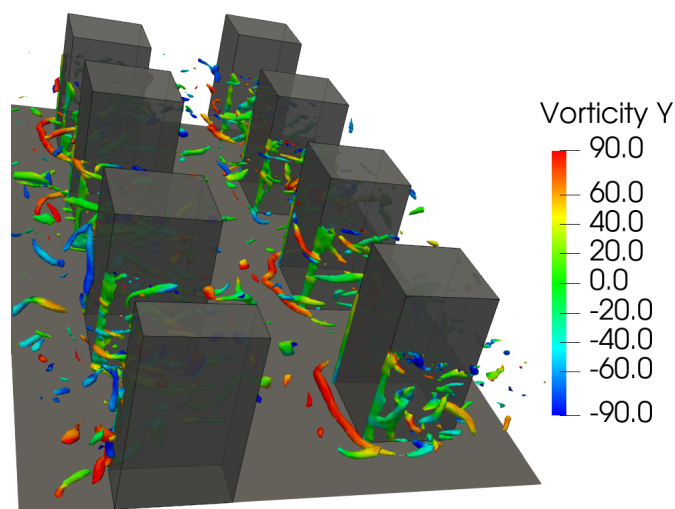


Figure 10. Q criterion colored by the y component of the vorticity.

Figure 11 plots 3D streamlines around the obstacle colored by the velocity y component. Wake structures can be visualized downstream from block. Furthermore, the streamlines also indicated outward interactions and sweep events occurring in the flow.

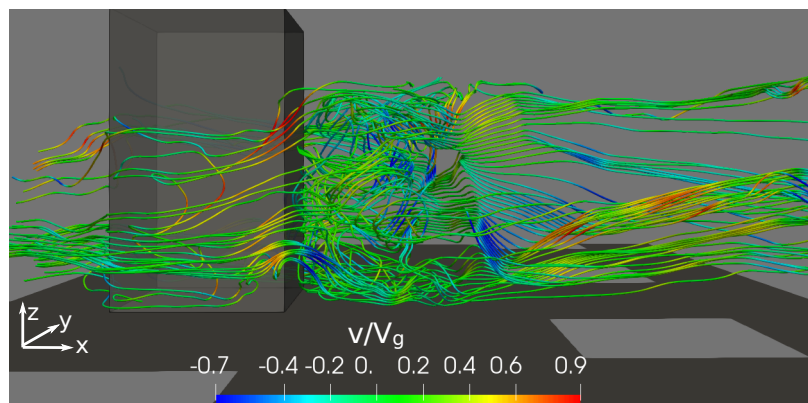


Figure 11. Streamlines around an obstacle colored with the velocity magnitude.

4.2. Validation: Case 2

For this second validation, the stage-discharge relationship was studied by focusing on the drag coefficient. Thus, the experimental and numerical mean water depths and discharges were used as inputs in Equation (2) to calculate C_d .

Figure 12 depicts the experimental and numerical results for the present study and, for comparison, the experimental results of two studies found in the literature. The circles (ADV circular) are from an investigation of a rock-ramp-type fish pass with circular obstacles performed by Cassan et al. [2]. The continuous line comes from the work of Baki et al. [3], who studied a rock-ramp-type fish pass with staggered arrangement of boulders with an approximately spherical shape. The continuous line corresponds to:

$$C_d = 1.787 \left(\frac{h}{D} \right)^{-2.16}, \tag{6}$$

which describes the fitted line to the measured points from [3].

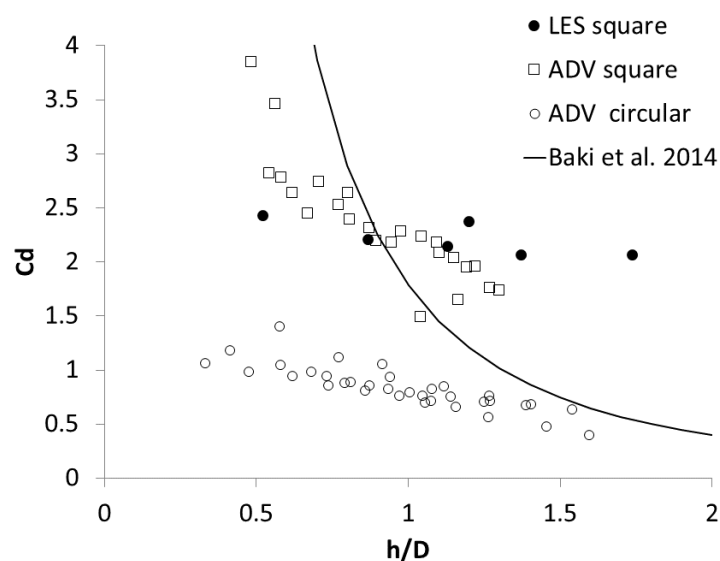


Figure 12. Drag coefficient for the stage-discharge study. The experimental results for the circular configuration (ADV circular) correspond to the study of Cassan et al. [2].

Figure 12 shows a clear dependency of C_d on the dimensionless water depth h/D . When the water depth was lower than the diameter, the flow pattern differed from the flow around an infinitely long obstacle. The bed interacted with the flow around the blocks, increasing the drag force. The same phenomenon was noticeable for circular ([2]) and square blocks. This phenomenon tended to be neglected when the water depth increased. As a consequence, the drag coefficient tended towards 1 for circular blocks and towards 2 for square obstacles. This behavior was not reached in fishways with macro roughness, which implied very large values of C_d . The boulders used by Baki et al. [3] had an intermediate shape, between circular and square, which explains the proposed correlation. Moreover, because for $h/D > 1$, the obstacles were submerged, the present results were only comparable with the correlation of Baki et al. [3] (Equation (6)) for $h/D < 1$.

The good agreement between experiment and numerical results allowed validating the simulation performed for several water depths. Therefore, it could be concluded that the validation done previously may be also correct for a larger range of configuration (Froude number and water depth).

4.3. Comparison between Square and Circular Obstacles

In this section, the flow properties computed from a simulation across staggered square obstacles are compared with the results obtained with staggered cylinders. For this aim, the study of Chorda et al. [1] was taken as a reference. In their work, the authors investigated a flow crossing staggered emergent cylinders in a concentration of $C = 16\%$, at a discharge of $Q = 0.05 \text{ m}^3/\text{s}$, and the mean water height was about 0.10 m. As described in Section 2, to reach such a volumetric flow rate, the initial water depth was set to 0.158 m for the square obstacle simulation. Because of the different water heights, the two cases had different V_g . It was 0.83 m/s for the circular case from the study of Chorda et al. [1], and a value of 0.53 m/s was assumed for the present case. The mean velocity field for the two cases can be seen in Figure 13.

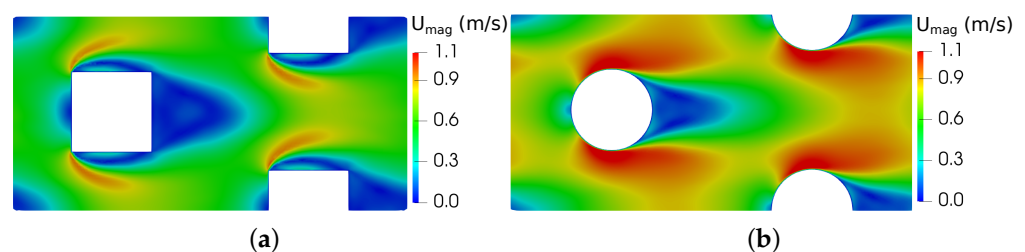


Figure 13. Mean velocity magnitude at $z/D = 0.47$. Results from the domain with square obstacles from the present work (a) and simulation with circular obstacles from Chorda et al. [1] (b).

The profiles of the three velocity components along Line 1 at plane $z/h = 0.4$ are presented in Figure 14. In general, the profiles for both simulations presented similar values and behavior. As expected, due to the difference in the water height, the axial velocity component for the simulation with the circular blocks was higher than for the square case. They reached about 0.9 m/s for the former and 0.73 m/s for the latter case, which corresponded to $1.08 V_g$ and to $1.38 V_g$, respectively. The profiles for the component v had relatively small values, being in absolute lower than 0.03 m/s ($0.036 V_g$ for the circular case and lower than $0.057 V_g$ for the square obstacles). Furthermore, the values for w varied between -0.06 and 0.11 m/s ($-0.07 V_g$ and $0.13 V_g$) for the circular case, and they varied from -0.07 to 0.07 m/s ($-0.13 V_g$ to $0.13 V_g$) for the simulation with square obstacles.

The profiles for Line 3 at plane $z/h = 0.4$ can be seen in Figure 15. The axial velocity component profiles reached their minimum at the center axis of the obstacles, and as for Line 1, the values were greater for the circular case. They varied from 0.06 to 0.94 m/s ($0.07 V_g$ to $1.13 V_g$) for the simulation with circular obstacles and from -0.07 to 0.62 m/s ($0.13 V_g$ to $1.17 V_g$) for the square simulation. The lateral and vertical components oscillated around zero for both simulations, but the amplitude was slightly smaller for the square case. The values of the lateral velocity component ranged from -0.2 to 0.23 m/s (-0.24

V_g to $0.28 V_g$) for the circular case, while they ranged from -0.15 to 0.15 m/s ($-0.28 V_g$ to $0.28 V_g$) for the configuration with square obstacles. For the vertical component, the values lied in between -0.05 and 0.11 m/s ($-0.06 V_g$ to $0.13 V_g$) for the simulation with circular obstacles, and they were between -0.08 and 0.05 m/s ($-0.15 V_g$ to $0.09 V_g$) for the simulation with square blocks.

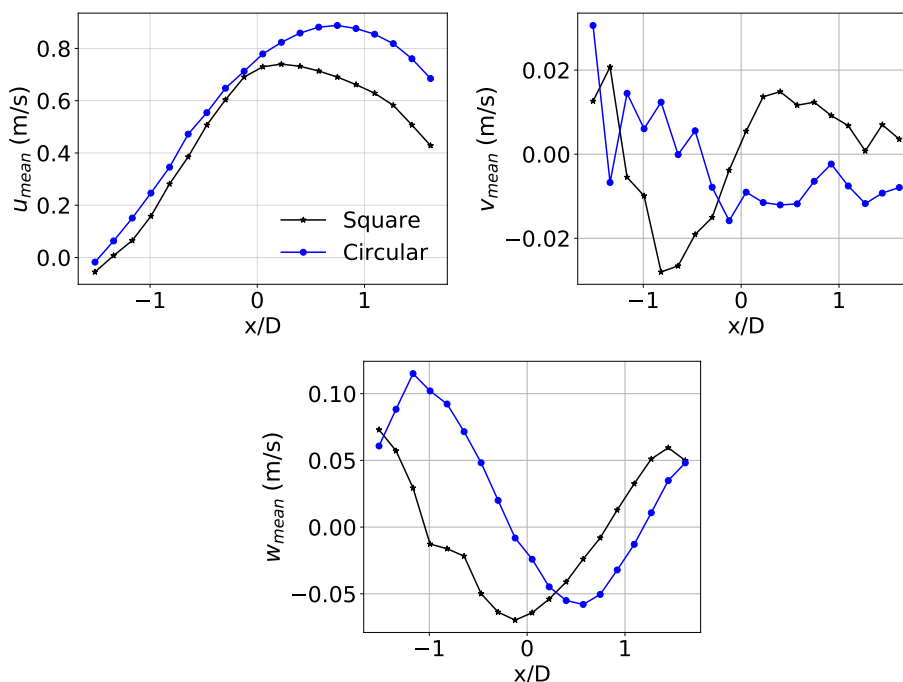


Figure 14. Mean velocity components along Line 1 at plane $z/h = 0.4$. The circles correspond to the simulation with circular obstacles reported by Chorda et al. [1].

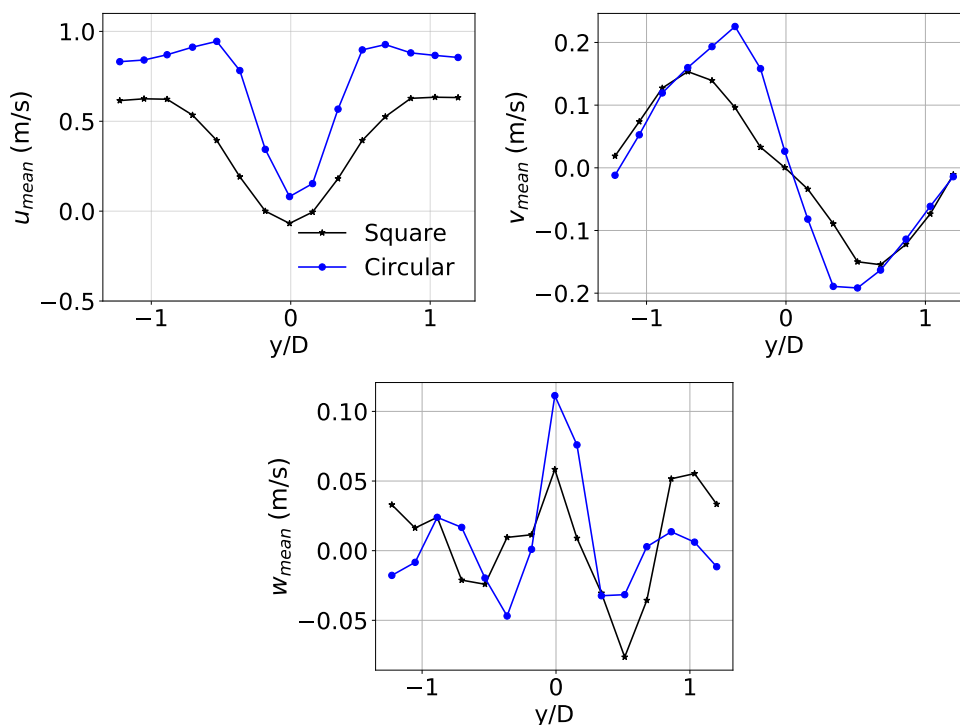


Figure 15. Mean velocity components along Line 3 at plane $z/h = 0.4$. The circles correspond to the simulation with circular obstacles reported by Chorda et al. [1].

Turbulent kinetic energy (k) profiles for the square and cylinder simulations (Figure 16) showed the turbulence level of the square simulation was lower than the circular one for almost all positions in both extracted lines. The maximum values were about $0.08 \text{ m}^2/\text{s}^2$ ($0.12 V_g^2$) for the circular simulation in the Line 1, while this value was about $0.06 \text{ m}^2/\text{s}^2$ ($0.21 V_g^2$) for the square case. For Line 2, the maximum value was about $0.09 \text{ m}^2/\text{s}^2$ ($0.13 V_g^2$) for the circular obstacles and approximately $0.05 \text{ m}^2/\text{s}^2$ ($0.18 V_g^2$) for the simulation with square obstacles.

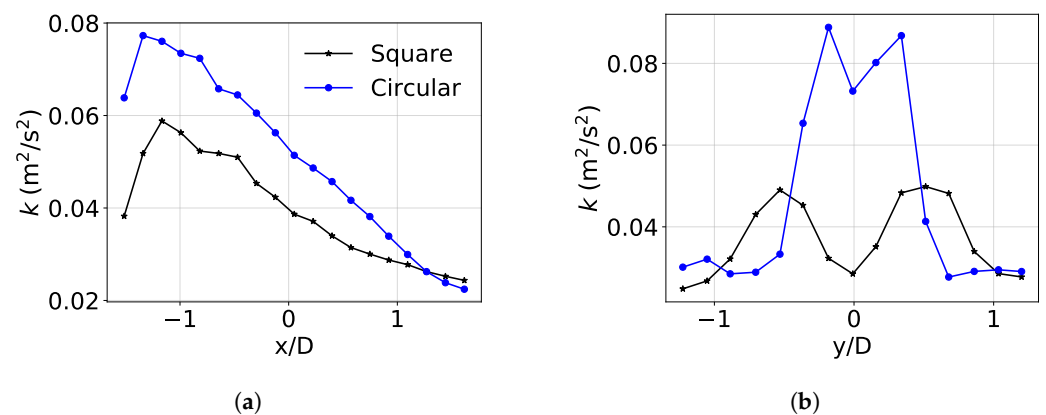


Figure 16. Turbulent kinetic energy at plane $z/h = 0.4$ along Lines 1 (a) and 3 (b). The circles correspond to the simulation with circular obstacles reported by Chorda et al. [1].

The depth-averaged turbulent kinetic energy was computed along Line 1 for both configurations, and the results are shown in Figure 17a. For both cases, it increased in the wake zone, reaching a maximum value, then it decreased gradually along the longitudinal line. This plot confirmed the larger wake zone for the square blocks. The values ranged from 0.027 to $0.065 \text{ m}^2/\text{s}^2$ (0.04 to $0.094 V_g^2$) for the configuration with circular cylinders and from 0.027 to $0.047 \text{ m}^2/\text{s}^2$ (0.096 to $0.167 V_g^2$) for the square blocks. To describe the curve, a power equation was applied fitting the points in the region after the wake zone, and the resulting fitted line is additionally depicted in Figure 17a.

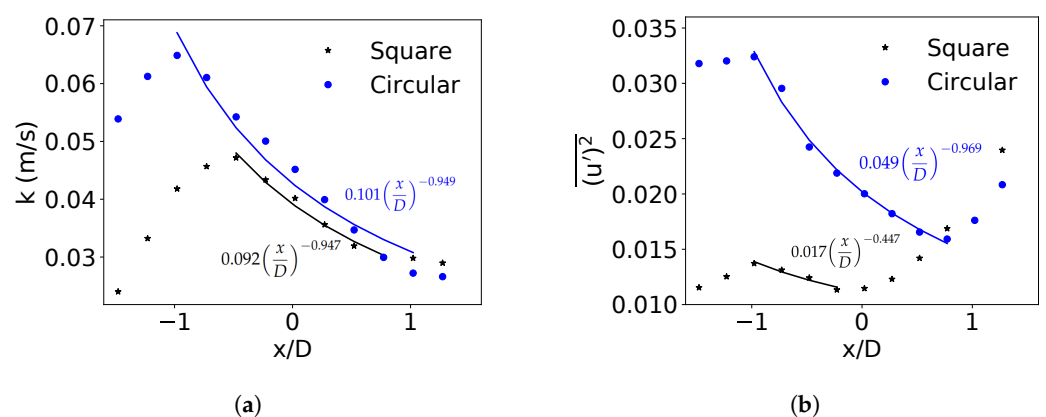


Figure 17. Square depth-averaged turbulent kinetic energy (a) and square depth-averaged streamwise turbulent intensity (b) along Line 1. The circles correspond to the simulation with circular obstacles reported by Chorda et al. [1].

The same procedure was performed for the streamwise turbulent intensity $\overline{(u')^2}$, and the results are plotted in Figure 17b. Along the considered Line 1, the values also increased in the wake zone. After, they gradually decreased, then they slowly rose again because of the downstream obstacle and the subsequent stagnation point. The values ranged from 0.012 to $0.024 \text{ m}^2/\text{s}^2$ (0.043 to $0.085 V_g^2$) for the square obstacles and from 0.016 to

$0.032 \text{ m}^2/\text{s}^2$ (0.023 to $0.046 V_g^2$) for the circular configuration. A fitted line to describe the variation after the wake zone is also shown in this plot.

The turbulent intensity is calculated as [14]:

$$I = \left(\frac{2}{3} \frac{k}{V_g^2} \right)^{0.5} \quad (7)$$

and depicted in Figure 18 for a plane at $z/D = 0.47$. The values of the intensity were between 10 and 40% for the simulation with the square obstacles and were between 10 and 35% for the circular cylinders. The highest values for the latter case were located in the wake zone while, and for the square simulation, they were found near the sides of the obstacles.

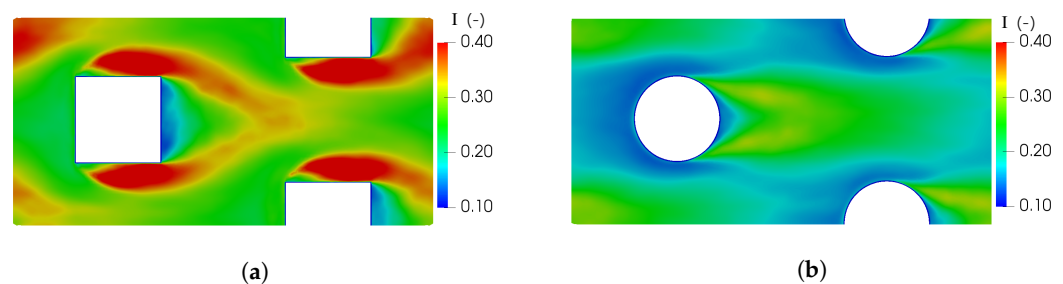


Figure 18. Turbulent intensity at $z/D = 0.47$. Results from the domain with square obstacles from the present work (a) and simulation with circular obstacles from Chorda et al. [1] (b).

As an important property affecting fish behavior, the lateral velocity component fluctuation v' was analyzed at the wake zone in four locations along the center axis of the obstacle at three vertical positions, $z/h = 0.16$, $z/h = 0.47$, and $z/h = 0.8$. The spectrum of v' , illustrated in Figure 19, presents the frequency of the vortices generated by the obstacle arrangement. The left side of Figure 19 shows the results for the square blocks' simulation from the present work, while on the right side, the results with circular cylinders from Chorda et al. [1] are presented. The values were normalized with the highest amplitude, which was obtained at the lowest vertical position $z/h = 0.16$ of the circular obstacles simulation. For the square obstacles, the line at $z/h = 0.8$ presented the highest amplitude, and it was given for $St = 0.35$ and $x/D = 2.0$. At lines $z/h = 0.16$ and $z/h = 0.47$, the highest amplitude was found at $x/D = 1.1$ and for $St = 0.24$ and $St = 0.25$, respectively. For the circular case, the highest amplitude was given for $St = 0.24$ and $x/D = 1.1$ at the vertical positions $z/h = 0.16$ and $z/h = 0.47$; while for $z/h = 0.8$, the highest values were also at $x/D = 1.1$, but $St = 0.35$.

The quadrant analysis of the velocity fluctuations u' and w' was performed in order to analyze the fractional contribution of the different bursting events to the uw component of the Reynolds shear stress. For this analysis, the profiles of $P_{I,H}$ along Line 1 at different vertical positions are plotted in Figure 20. For higher vertical positions ($z/h = 0.47$ and $z/h = 0.8$), outward and inward events were dominant for the majority of the collected points for both simulations, and the higher the position, the greater was the importance of outward interactions. The fractional distribution of the events in these positions differed from the one found in the region close to the bottom ($z/h = 0.16$). For this position, ejections and sweep events were dominant at almost all x positions for the simulation with square obstacles. For the same vertical position, outward and sweep events were dominant downstream of the obstacle for the circular cylinders until approximately $x/D = -1$. Then, inward and ejection events became more important, except for the point immediately upstream of the obstacle, where outward events were more frequent. The dominance of burst events in the region close to the bottom was expected. According to Lu and Willmarth [26], throughout the turbulent boundary layer, the bursts (sweep and ejection) were the largest contributors to $\overline{u'w'}$.

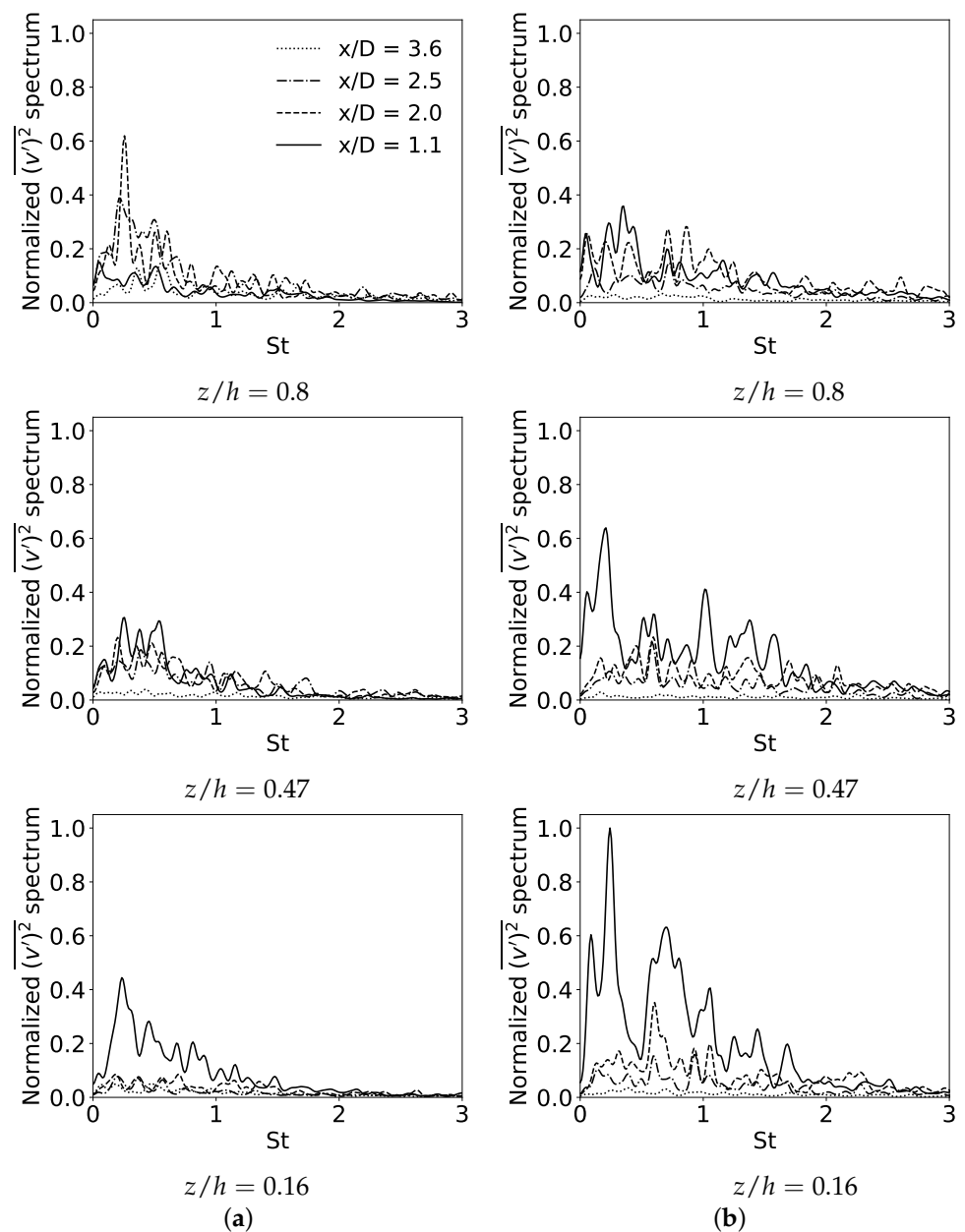


Figure 19. Spectrum of the lateral fluctuations as a function of the Strouhal number at Line 1 for different vertical positions. Results from domain with square obstacles (a) and simulation with circular obstacles from Chorda et al. [1] (b).

The distribution of the Reynolds shear stress component $\overline{u'w'}$ is plotted in Figure 21. Following the quadrant analysis, $\overline{u'w'} > 0$ corresponds to a region where inward or outward interactions events are dominant, while for $\overline{u'w'} < 0$, sweep or ejections are more frequent. These plots show the dominance of inward or outward interactions in the wake zone, confirming the results of the quadrant analysis. By comparing the two simulations, regions with negative values of $\overline{u'w'}$, which corresponds to burst events, were more common in the simulations with the square obstacles.

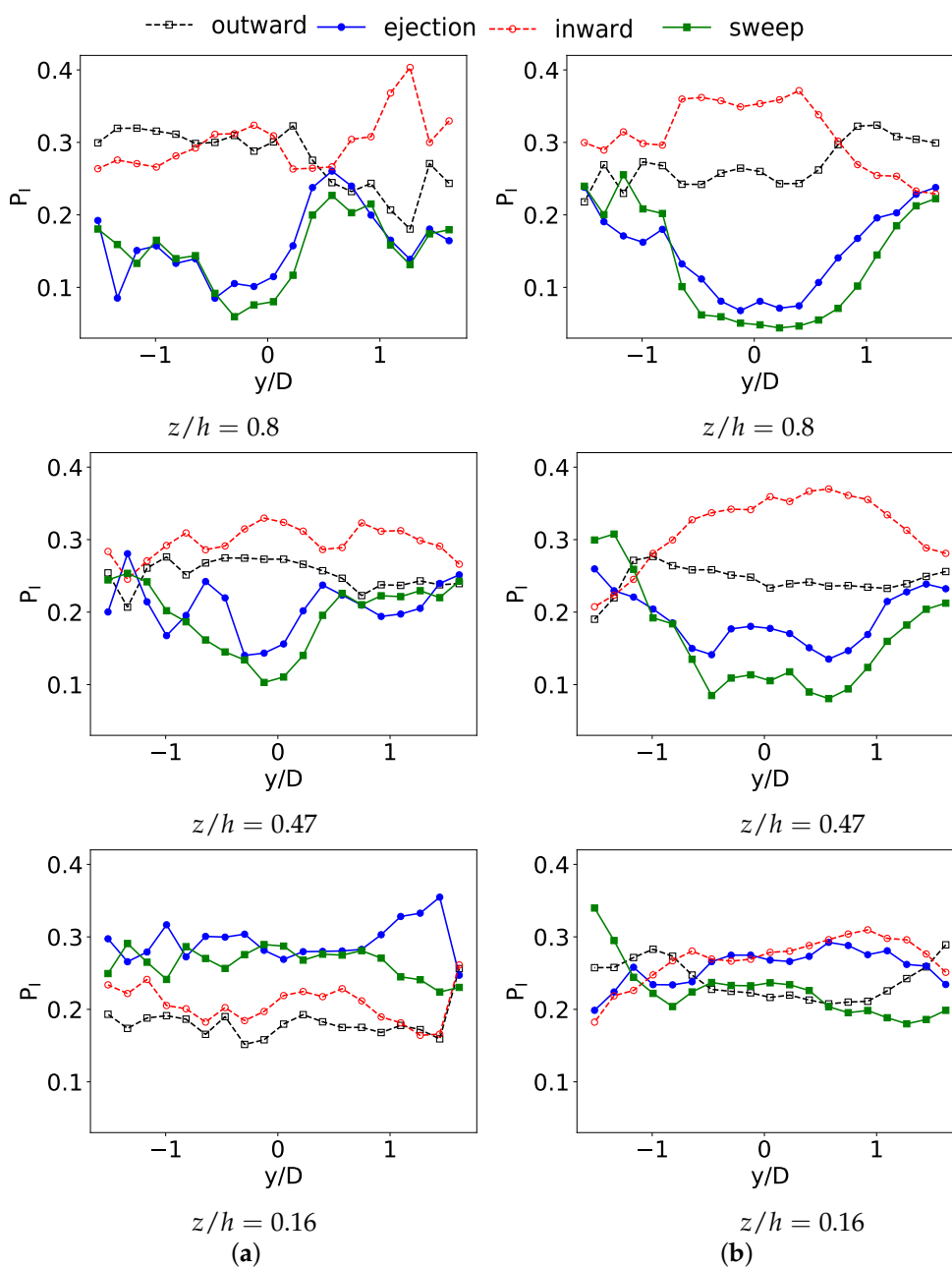


Figure 20. Proportion of the joint turbulent event distribution along Line 1 at different vertical positions. Results from domain with square obstacles (a) and simulation with circular obstacles from Chorda et al. [1] (b).

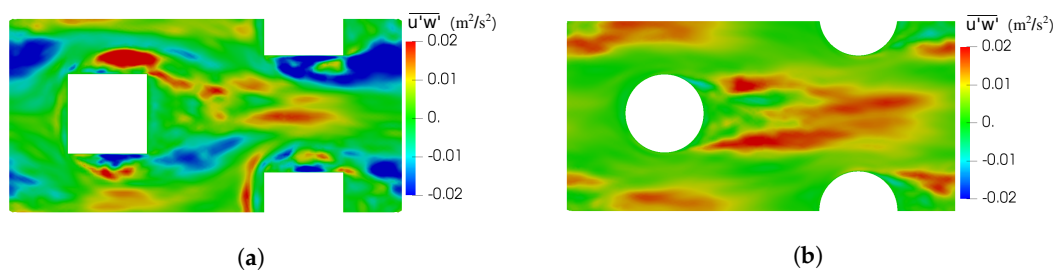


Figure 21. Reynolds shear stress component $\overline{u'w'}$ at $z/D = 0.47$. Results from domain with square obstacles from the present work (a) and simulation with circular obstacles from Chorda et al. [1] (b).

It is important to point out that the results from the simulation with circular obstacles depicted in Figures 18–21 were not shown in the publication of Chorda et al. [1], but they were post-processed from the results of their simulation published in the referenced article.

5. Discussion

By analyzing the depth-averaged turbulent kinetic energy in Figure 17a, it was shown that the region after the wake zone presented a decay exponent of approximately -0.95 for both configurations. Similar results were found by Baki et al. [8]. In their paper, the authors investigated a rock-ramp-type fish pass with a staggered arrangement of boulders with an approximately spherical shape. They computed a decay exponent for the square depth-averaged turbulent kinetic energy (\sqrt{k}) of about -0.5 , which corresponded to a decay exponent of about -1.0 if k was considered instead of its square root. The values for the depth-averaged turbulent kinetic energy varied from 9.6 to 16.7% of V_g^2 for the square obstacles and from 4 to 9.4% of V_g^2 for the circular blocks. These results were consistent with the findings of Baki et al. [8]. In their study, these values ranged from 2.2 to 12.2% of the square of the maximum flow velocity.

For the depth-averaged streamwise turbulence intensity in Figure 17b, the decay exponent was -0.45 for the square case and -0.97 for the circular obstacles. The decay exponent for the configuration with circular cylinders was similar to those found in the literature ([8,27,28]). Nosier et al. [27] studied the characteristics of the wake generated by twin cylinders arranged in parallel side-by-side and staggered arrangements. They computed a decay exponent of -1.0 . This value was also the one resulting from a single-cylinder wake ([27,28]). For the study with approximately spherical boulders of Baki et al. [8], the corresponding decay exponent for the depth-averaged streamwise turbulence intensity was also approximately -1.0 . Nevertheless, in the present paper, a significant smaller decay exponent (-0.45) was found for the square blocks. This indicated that the components $\overline{(v')^2}$ and $\overline{(w')^2}$ may play a more significant role in the wake zone for the configuration with square blocks than in the one for circular cylinders. The values for the depth-averaged streamwise turbulence intensity ranged from 4.3 to 8.5% of V_g^2 for the square obstacles and from 2.3 to 4.6% of V_g^2 for the circular blocks. These values were also consistent with the ones found in the work of Baki et al. [8]. Their corresponding values varied from 2.2 to 9.0% of the square of the maximum flow velocity.

As discussed in Tran et al. [14], areas of low speed and low turbulence can increase the passage efficiency. As shown above, the same discharge in a configuration with square blocks presented a lower turbulent intensity and lower lateral fluctuations than with circular obstacles. However, it could also involve an increase of almost 60% of the water depth. Because of building constraints, the water depth had to be reduced. On the other hand, the attractiveness of the fish pass had to be maintained by a sufficient discharge. This showed that the shape is an important modifiable parameter, as well as the density and the diameter to be taken into account when designing this type of fish pass.

As given in Equation (2), when parameters such as slope, concentration, obstacle diameter, and water depth are the same, the relation between the discharges of the configurations with square and circular blocks is approximately:

$$\frac{Q_{\text{square}}}{Q_{\text{circular}}} \approx \sqrt{\frac{Cd_{\text{square}}}{Cd_{\text{circular}}}} \quad (8)$$

Remembering that $Cd_{\text{square}} \approx 2$ and $Cd_{\text{circular}} \approx 1$, the discharge would be smaller for the square configuration, which reduced its attractiveness. Nevertheless, this also means that the velocity between the blocks was drastically reduced, which indicated a better passability of the fish pass with square obstacles. In addition, by comparing the wake regions, the wake for the configuration with square obstacles was larger and quieter than the wake for circular blocks. For instance, considering an averaged intensity of 20% for both cases in the wake (Figure 18), k was $0.085 \text{ m}^2/\text{s}^2$ for the circular block wake and

$0.05 \text{ m}^2/\text{s}^2$ for the square block wake. This comparison pointed out once more that the wake developed from square obstacles was more adequate for fish rest. Therefore, square blocks had significant advantages in terms of reduced velocity and turbulence, but they had also a less attractive discharge. The configuration to be employed had to be chosen according to the site configuration: competing discharge, position of the fish pass entrance, etc.

According to Triantafyllou et al. [29], the propulsive efficiency for aquatic animals corresponded to the interval: approximately $0.25 < St < 0.35$. Thus, the spectra of lateral velocity fluctuations could help in the estimation of unsteady movements relative to fish. For both geometries, the spectra showed a similar behavior in relation to the Strouhal number, with peaks located at $St = 0.24 - 0.25$. They differed only for higher vertical positions, which should not impact the fish behavior.

Turbulent events play an important role in sediment transport and resuspension [10]. According to Golpira et al. [11], the lack of frequent sweep events, as in the wake zone, may imply a higher sediment deposition. In addition, the low frequency of ejections and sweeps events, as seen in Figure 20, could indicate preferential paths of resting zones for fish. Sediment deposition is unlikely to occur in the present fishway. However, the design process remains pertinent for by-pass rivers where the slope can be weaker and the deposition has to be taken into account. Further investigations are necessary to identify the fish preferences relatively to the turbulence events.

In general, knowledge about the local flow variations gained from the investigation of Chorda et al. [1] and the present study ensures that the design process based on integrated values as the water depth and the discharge is pertinent for fish passages. Furthermore, as could be seen in the two validation cases shown in this work, the simulation with the LES model of this type of flow was satisfactory. As investigated in Chorda et al. [1], with the RANS methodology, this high turbulent flow could hardly be reproduced with such accuracy and details as with LES.

6. Conclusions

In this work, a rock-ramp fish pass with square blocks was experimentally and numerically investigated. Shadowgraphy was employed for measuring the water depth, and the velocity profiles were obtained with ADV. For the simulations, the open-source code OpenFOAM was employed. LES was applied as the turbulence model, and the multiple phases were treated with the VOF method. In addition, the cyclic boundary condition was applied to reduce the computational cost.

In the first part of this paper, two different validations were successfully performed. In the first one, the numerical results regarding the velocity field and turbulent kinetic energy were compared with the measurements. In the second validation, the experimental and numerical stage-discharges were compared. Both comparisons presented a satisfactory agreement. In the second part of this study, the turbulence characteristics resulting from a rock-ramp fish pass with square obstacles were compared with the ones resulting from a passage with circular obstacles. For this investigation, the discharge was nearly the same for both configurations, which implies different water depths for both geometries. The results showed a lower velocity field and a lower turbulent kinetic energy for the square obstacles. However, this configuration also presented the highest water depth. In addition, the results for the depth-averaged turbulent kinetic energy and depth-averaged streamwise turbulent intensity presented similar values as the ones found in the literature. The analysis of the Strouhal number of the lateral velocity fluctuations showed similar results between the two cases. Furthermore, no significant discrepancies between the two domains were observed in the quadrant analysis. Finally, the Reynolds shear stress component $\overline{u'w'}$ fields were compared, and the results showed more burst areas in the simulation with square obstacles. In general, the results prove that the obstacle shape is an important modifiable parameter for designing this type of fishway.

Author Contributions: Conceptualization, L.C. and F.C.M.; methodology, L.C., P.L., T.D.T., and F.C.M.; software, L.C. and F.C.M.; validation, L.C. and F.C.M.; formal analysis, L.C. and F.C.M.; investigation, L.C. and F.C.M.; resources, L.C. and P.L.; data curation, L.C., T.D.T. and F.C.M.; writing—original draft preparation, L.C. and F.C.M.; writing—review and editing, P.L. and T.D.T.; visualization, F.C.M. and L.C.; supervision, L.C.; project administration, L.C. and P.L.; funding acquisition, L.C. and P.L. All authors read and agreed to the published version of the manuscript.

Funding: This research was funded by Office Français pour la Biodiversité: convention pole écohydraulique OFB/IMFT/PPRIME.

Institutional Review Board Statement: Not applicable.

Informed Consent Statement: Not applicable.

Acknowledgments: The calculations were performed on the EOS supercomputer at CALMIP, Toulouse, France, which is gratefully acknowledged.

Conflicts of Interest: The authors declare no conflict of interest.

Appendix A

Tables A1 and A2 show the parameters of the stage-discharge validation for the measurements and simulation, respectively.

Table A1. Summary of the experimental parameters for the stage-discharge validation.

Slope S (%)	Discharge Q (m ³ /s)	Mean Water Depth h (m)
1	0.01	0.077
1	0.02	0.120
1	0.03	0.151
1	0.04	0.169
2	0.01	0.064
2	0.02	0.103
2	0.03	0.134
2	0.04	0.160
2	0.05	0.170
3	0.01	0.056
3	0.02	0.092
3	0.03	0.126
3	0.04	0.150
3	0.05	0.169
4	0.01	0.053
4	0.02	0.081
4	0.03	0.109
4	0.04	0.137
4	0.05	0.152
4	0.06	0.175
5	0.01	0.045
5	0.02	0.071
5	0.03	0.100
5	0.04	0.127
5	0.05	0.146
5	0.06	0.161
6	0.01	0.04
6	0.02	0.067
6	0.03	0.093
6	0.04	0.120
6	0.05	0.140
6	0.06	0.152

Table A1. Cont.

Slope S (%)	Discharge Q (m ³ /s)	Mean Water Depth h (m)
7	0.02	0.062
7	0.03	0.089
7	0.04	0.112
7	0.05	0.132
7	0.06	0.145

Table A2. Summary of the parameters employed in the simulations for the stage-discharge validation.

Slope S (%)	Initial Water Depth h (m)	Discharge Q (m ³ /s)
5	0.060	0.0178
5	0.100	0.0311
5	0.130	0.041
5	0.158	0.051
5	0.200	0.0643

References

- Chorda, J.; Cassan, L.; Laurens, P. Modeling Steep-Slope Flow across Staggered Emergent Cylinders: Application to Fish Passes. *J. Hydraul. Eng.* **2019**, *145*, 1–14. [[CrossRef](#)]
- Cassan, L.; Tien, T.; Courret, D.; Laurens, P.; Dartus, D. Hydraulic resistance of emergent macroroughness at large Froude numbers: Design of nature-like fishpasses. *J. Fluids Struct.* **2014**, *140*, 1–9. [[CrossRef](#)]
- Baki, A.B.M.; Zhu, D.Z.; Rajaratnam, N. Mean Flow Characteristics in a Rock-Ramp-Type Fish Pass. *J. Hydraul. Eng.* **2014**, *140*, 156–168. [[CrossRef](#)]
- Tritico, H.M.; Cotel, A.J. The effects of turbulent eddies on the stability and critical swimming speed of creek chub (*Semotilus atromaculatus*). *J. Exp. Biol.* **2010**, *213*, 2284–2293. [[CrossRef](#)]
- Tan, J.; Tao, L.; Gao, Z.; Dai, H.; Shi, X. Modeling Fish Movement Trajectories in Relation to Hydraulic Response Relationships in an Experimental Fishway. *Water* **2018**, *10*, 1511. [[CrossRef](#)]
- Cotel, A.J.; Webb, P.W. Living in a Turbulent World—A New Conceptual Framework for the Interactions of Fish and Eddies. *Integr. Comp. Biol.* **2015**, *55*, 662–672. [[CrossRef](#)]
- Oertel, M.; Peterseim, S.; Schlenkhoff, A. Drag coefficients of boulders on a block ramp due to interaction processes. *J. Hydraul. Eng.* **2011**, *49*, 372–377. [[CrossRef](#)]
- Baki, A.B.M.; Zhu, D.Z.; Rajaratnam, N. Turbulence Characteristics in a Rock-Ramp-Type Fish Pass. *J. Hydraul. Eng.* **2015**, *141*, 1–14. [[CrossRef](#)]
- Baki, A.B.M.; Zhu, D.Z.; Rajaratnam, N. Flow Structures in the Vicinity of a Submerged Boulder within a Boulder Array. *J. Hydraul. Eng.* **2016**, *143*, 1–13. [[CrossRef](#)]
- Golpira, A.; Huang, F.; Baki, A.B.M. The Effect of Habitat Structure Boulder Spacing on Near-Bed Shear Stress and Turbulent Events in a Gravel Bed Channel. *Water* **2020**, *12*, 1423. [[CrossRef](#)]
- Golpira, A.; Baki, A.B.; Zhu, D.Z. Higher-order Velocity Moments, Turbulence Scales and Energy Dissipation Rate around a Boulder in a Rock-ramp Fish Passage. *Sustainability* **2020**, *12*, 5385. [[CrossRef](#)]
- Baki, A.B.M.; Zhu, D.Z.; Rajaratnam, N. Flow Simulation in a Rock-Ramp Fish Pass. *J. Hydraul. Eng.* **2016**, *142*, 1–12. [[CrossRef](#)]
- Tseng, M.H.; Yen, C.L.; Song, C.C.S. Computation of three-dimensional flow around square and circular piers. *Int. J. Numer. Methods Fluids* **2000**, *34*, 207–227. [[CrossRef](#)]
- Tran, T.D.; Chorda, J.; Laurens, P.; Cassan, L. Modelling nature-like fishway flow around unsubmerged obstacles using a 2D shallow water model. *Environ. Fluid Mech.* **2016**, *16*, 413–428. [[CrossRef](#)]
- Larinier, M.; Courret, D.; Gomes, P. Technical Guide to the Concept on Nature-Like Fishways. *Rapport GHAAPPE RA.06.05-V1*. 2006. Available online: http://www.trameverteetbleue.fr/sites/default/files/references_bibliographiques/guide_passes_poissons.pdf (accessed on 23 April 2021).
- Smagorinsky, J. General circulation experiments with the primitive equations, 1. the basic experiment. *Mon. Weather Rev.* **1963**, *91*, 99–164. [[CrossRef](#)]
- Hirt, C.W.; Hirt, B.N. Volume of fluid (VOF) method for the dynamics of free boundaries. *J. Comput. Phys.* **1981**, *39*, 201–225. [[CrossRef](#)]
- Greenshields, C.J. *OpenFOAM User Guide*; OpenFOAM Foundation Ltd. 2020. Available online: <http://foam.sourceforge.net/docs/Guides-a4/OpenFOAMUserGuide-A4.pdf> (accessed on 23 April 2021).
- Cassan, L.; Laurens, P. Design of emergent and submerged rock-ramp fish passes. *Knowl. Manag. Aquat. Ecosyst.* **2016**, *417*, 1–10. [[CrossRef](#)]

20. Ducrocq, T.; Cassan, L.; Chorda, J.; Roux, H. Flow and drag force around a free surface piercing cylinder for environmental applications. *Environ. Fluid Mech.* **2017**, *17*, 629–645. [[CrossRef](#)]
21. Lacey, R.W.J.; Roy, A.G. Fine-Scale Characterization of the Turbulent Shear Layer of an Instream Pebble Cluster. *J. Hydraul. Eng.* **2008**, *134*, 925–936. [[CrossRef](#)]
22. Pope, S. Ten questions concerning the large-eddy simulation of turbulent flows. *New J. Phys.* **2004**, *6*, 1–24. [[CrossRef](#)]
23. Lacey, R.W.J.; Rennie, C.D. Laboratory Investigation of Turbulent Flow Structure around a Bed-Mounted Cube at Multiple Flow Stages. *J. Hydraul. Eng.* **2012**, *71*, 71–84. [[CrossRef](#)]
24. Martinuzzi, R.; Tropea, C. Flow around surface-mounted, prismatic obstacles placed in a fully developed channel flow. *J. Fluids Eng.* **1993**, *115*, 85–92. [[CrossRef](#)]
25. Larousse, A.; Martinuzzi, R.; Tropea, C. Flow Around Surface-Mounted, Three-Dimensional Obstacles. In Proceedings of the 8th Symposium on Turbulent Shear Flows, Munich, Germany, 9–11 September 1991.
26. Lu, S.S.; Willmarth, W.W. Measurements of the structure of the Reynolds stress in a turbulent boundary layer. *J. Fluids Mech.* **1973**, *60*, 481–511. [[CrossRef](#)]
27. Nosier, M.A.; Elbaz, A.R.; Fetouh, T.N.A.; El-Gabry, L.A. Characteristics of turbulent wakes generated by twin parallel cylinders. *J. Fluids Eng.* **2012**, *134*, 121201–121210. [[CrossRef](#)]
28. Tennekes, H.; Lumley, J.L. *A First Course in Turbulence*; MIT Press: Cambridge, MA, USA, 1972.
29. Triantafyllou, G.S.; Triantafyllou, M.S.; Gosenbaugh, M.A. Optimal Thrust Development in Oscillating Foils with Application to Fish Propulsion. *J. Fluids Struct.* **1993**, *7*, 205–224. [[CrossRef](#)]